# The Potential of Lithium Metasilicate Glass in Bioinspired Zirconia Infiltration Technology: An Experimental Study

**Mohsen Sadeghpour Motlagh[1], Sara Banijamali[1*], Bijan Eftekhari Yekta[2]**

*1. Ceramic Department, Materials and Energy Research Center (MERC), Karaj, Iran.*

*2. Ceramic Division, School of Materials and Metallurgy Engineering, Iran University of Science and Technology, Tehran, Iran.*

**(*Corresponding author: banijamali@merc.ac.ir, banijamalis@yahoo.com)**





[ DOI: 10.22068/ijmse.4363 ]

**Abstract**

This study investigates the crystallization behavior and microstructural evolution of lithium metasilicate ($Li_2SiO_3$) glass subjected to thermal histories designed to emulate the cooling stage of zirconia infiltration in dental restorations. Three thermal routes were examined: (i) a non-isothermal schedule to identify crystallization and melting events, (ii) a controlled isothermal schedule to obtain homogeneous glass–ceramic microstructures, and (iii) a quasi-isothermal natural cooling schedule from the molten state to mimic the thermal profile during infiltration without reproducing actual capillary flow or interfacial reactions. Phase identification and quantitative analysis were performed by X-ray diffraction with Rietveld refinement, and the resulting microstructures were characterized by field-emission scanning electron microscopy. Under isothermal conditions, lithium metasilicate ($Li_2SiO_3$), lithium disilicate ($Li_2Si_2O_5$), γ-spodumene (γ-$LiAlSi_2O_6$), β-lithium phosphate (β-$Li_3PO_4$), and quartz crystallized with an overall crystallized fraction of approximately 62±0.9 wt.%. In contrast, quasi-isothermal cooling produced a crystallized fraction exceeding 87±1 wt.%, dominated by lithium metasilicate ($Li_2SiO_3$), β-lithium phosphate, quartz, and cristobalite, with neither lithium disilicate ($Li_2Si_2O_5$) nor γ-spodumene (γ-$LiAlSi_2O_6$) detected under the present XRD conditions. The quasi-isothermal route also generated significantly coarser morphologies: average crystal length and thickness were roughly 10-fold and 31-fold larger, respectively, than those in the isothermally treated sample. These results demonstrate that the thermal path strongly governs phase assemblage, crystallized volume fraction, and crystal morphology in lithium silicate glass–ceramics. By clarifying how controlled versus quasi-isothermal cooling histories shape the final microstructure, this work provides a structural basis for optimizing lithium silicate glasses used in zirconia infiltration



[ DOI: 10.22068/ijmse.4363 ]

technology and for guiding future studies on the mechanical and functional performance of these materials.

**Keywords:** Lithium metasilicate glass-ceramics; thermal treatment pathways; crystallization; microstructure; glass infiltration; all-ceramic restorations.

## 1. Introduction

The design and fabrication of high-performance and naturally aesthetic dental restorations have always been key challenges in restorative dentistry. All-ceramic monolithic restorations have recently become an attractive option for replacing metal-ceramic restorations due to their favorable optical properties, high biocompatibility, and aesthetic appeal [1-4]. However, achieving a balance between mechanical properties, processability, and aesthetics remains an open issue [5-9]. In this context, the novel glass infiltration technique into a porous zirconia framework has been introduced as a bioinspired (biomimetic) approach to overcome traditional limitations. In this method, the infiltration of a low-viscosity glass into the porous zirconia structure forms a gradient structure in terms of composition and elastic modulus. This structure not only improves stress distribution and enhances mechanical strength but also significantly elevates the optical properties and aesthetics of the restoration by creating a glass surface layer [10-14]. This glass surface layer increases the fracture resistance of the restoration by reducing surface stresses and preventing crack propagation [15-21]. At the same time, by reducing antagonist teeth, protects the zirconia from the moist oral environment and enhances bond strength with resin adhesives due to increased etch-ability, ensuring the long-term stability of the restoration [22-26].





[ DOI: 10.22068/ijmse.4363 ]

Previously, the main focus in the infiltration process within porous zirconia frameworks was on the use of amorphous glasses. In these studies, compositions such as lanthanide glasses [27-29], borosilicate glasses [30, 31], and aluminosilicate glasses [32-34] were utilized, which retained their non-crystalline structure after infiltration. These glasses were considered suitable for dental applications due to their high chemical stability, tunable thermal expansion coefficients, relatively low melting temperatures that provide high melt fluidity, and the ability to control color through compositional adjustments, enabling effective filling of zirconia framework porosities during infiltration. However, in recent years, a novel approach has been emerging that focuses on the use of glasses with controlled crystallization capabilities, particularly in lithium silicate-based systems. These systems, due to their ability to engineer crystalline structures, enhanced mechanical properties, and good compatibility with dental zirconia, have opened new horizons in the development of infiltrative materials for all-ceramic restorations.

In this context, the glass-ceramics present in the lithium silicate system, especially lithium disilicate ($Li_2Si_2O_5$), have been proposed as one of the most promising options for infiltration into porous zirconia. This material, which has previously been widely used in monolithic dental restorations [35], demonstrates reliable performance in dental environments due to its features such as high optical transparency [36], favorable biocompatibility [37], good strength and fracture toughness [38], and controllable crystallization [39]. These unique properties have drawn researchers' attention to the possibility of using it in infiltration technology, to the extent that in a pioneering study, this glass was tested for the first time in the infiltration process into porous zirconia [21]. However, in that research, the crystallization behavior of the glass during and after the infiltration process and its impact on the final structure and functional properties of the restorative material were not investigated.





[ DOI: 10.22068/ijmse.4363 ]

One of the emerging glass-ceramics in the lithium silicate system that has recently been developed by Zanotto and colleagues [40, 41] is lithium metasilicate ($Li_2SiO_3$) glass-ceramic; a composition with high fracture toughness, significant mechanical strength, and suitable machinability. Unlike the common glasses in this system, whose final phase is lithium disilicate ($Li_2Si_2O_5$), in this composition, the predominant phase after crystallization remains lithium metasilicate ($Li_2SiO_3$). By carefully designing the initial composition and applying an engineered thermal cycle, this phase can be stabilized as a final stable structure. This glass-ceramic not only possesses flexural strength and fracture toughness at the level of lithium disilicate ($Li_2Si_2O_5$) but also has suitable machinability during the CAD/CAM stage and creates a crack-resistant microstructure after crystallization [40, 41]. An important advantage of this composition is its lower melting temperature and lower viscosity of the melt, which allows the infiltration process to occur at lower temperatures, reduces the risk of undesirable phase changes in zirconia, facilitates the melt's penetration into the micro-pores of the zirconia framework, and simplifies thermal cycle control; factors that collectively can improve the quality and durability of the final structure.

Despite these advantages, there has yet to be a report on the practical use of lithium metasilicate ($Li_2SiO_3$) glass-ceramic in the infiltration process in porous dental zirconia frameworks. Therefore, there exists a significant research gap in understanding the behavior of this material under thermal conditions similar to those of infiltration. Therefore, the aim of the present study is to investigate how uncontrolled thermal treatment conditions specifically natural cooling from the melt to room temperature inside the furnace affect the crystallization pathway and microstructural evolution of lithium metasilicate ($Li_2SiO_3$) glass. These thermal conditions were selected to reproduce only the thermal profile of the cooling stage in zirconia glass-infiltration processes, without conducting practical infiltration or evaluating mechanical performance. The outcomes of





[ DOI: 10.22068/ijmse.4363 ]

this work are compared with fully controlled (isothermal) heat-treatment conditions derived from DTA analysis to clarify how different thermal histories govern phase formation and microstructure. To the best of our knowledge, no previous study has systematically examined lithium metasilicate ($Li_2SiO_3$) glass under quasi-isothermal cooling conditions simulating the thermal behavior associated with infiltration processes.

## 2- Materials and Methods

### 2-1 Preparation of Glass and Glass-Ceramics in the $Li_2O$-$SiO_2$ System

A glass with the chemical composition (in molar percentages) of 52.6 $SiO_2$ - 40.2 $Li_2O$ - 1.6 $B_2O_3$ - 1.4 CaO - 1.4 $TiO_2$ - 0.8 $P_2O_5$ - 0.6 $Al_2O_3$ - 0.4 $ZrO_2$ - 0.4 ZnO - 0.3 $K_2O$ - 0.2 SrO - 0.2 BaO was prepared from laboratory-grade chemicals. The raw materials were carefully weighed and then thoroughly mixed to achieve the desired homogeneity. The resulting homogeneous mixture was placed in a high-purity silica crucible and melted in an electric furnace at 1250°C for 30 minutes to obtain a homogeneous melt. To investigate the behavior of the glass after the melting process, three different thermal protocols were applied, the details of which are provided below. In the first pathway, a portion of the molten glass was immediately quenched in distilled water to obtain a fritted sample with an amorphous structure. The purpose of this step was to assess the amorphous nature of the sample and to examine its crystallization behavior using differential thermal analysis (DTA). The DTA test was conducted to determine key temperatures, including the glass transition temperature (Tg), crystallization temperature, melting temperature, and to identify potential polymorphic transformations. To study phase transformations at the specified endothermic and exothermic temperatures indicated in the DTA curve, approximately 5 grams of the amorphous





[ DOI: 10.22068/ijmse.4363 ]

glass powder were transferred to a furnace at the corresponding temperature and subjected to non-isothermal heat treatment for 30 minutes. After the thermal process, the samples were rapidly cooled in air and analyzed for phase content using X-ray diffraction (XRD). In the second pathway, a portion of the glass melt was poured into a pre-heated stainless-steel mold with dimensions of 10 mm x 50 mm x 50 mm. To relieve stress and eliminate thermal history, the sample was immediately transferred to a furnace set at 475°C, corresponding to the glass transition temperature ($T_g$) of the glass in question. The sample was held at this temperature for 2 hours and then naturally cooled in the furnace to ambient temperature. In the next step, the resulting glass block was cut into pieces with final dimensions of 3 x 4 x 30 $mm^3$ (with an accuracy of ±0.2 mm) using a low-speed diamond saw with a water-cooling system. These dimensions were selected according to ISO 6872 standards for three-point Flexural strength testing of dental ceramics. After cutting, the surfaces of the samples were polished sequentially using silicon carbide sandpaper with grit sizes of 320, 600, 800, 1200, 2000, 2500, and 3000 in the presence of water, and finally finished with a diamond paste of 0.3 microns. The samples were divided into two groups:

Group One: Without any additional thermal treatment, these served as bulk glass samples for characterization tests. These samples are referred to in the text with the suffix code "LS-Glass."

Group Two: These were subjected to isothermal heat treatment at temperatures extracted from the DTA test (corresponding to the temperatures for nucleation and growth of desired crystalline phases). In this phase, the samples were heated at a rate of 10°C/min to temperatures of 549°C and 711°C, and after holding for 120 minutes at each temperature, they were naturally cooled in the furnace. These samples are referred to in the text with the suffix code "LS-HT."

In the third pathway, the experiment was designed to simulate only the thermal cooling profile associated with infiltration processes, without performing actual glass infiltration, capillary flow,





[ DOI: 10.22068/ijmse.4363 ]

wetting, or interfacial reactions with zirconia. Accordingly, a portion of the molten glass was poured into a stainless-steel mold (50 × 50 × 10 mm³) preheated to 1000 °C, and immediately transferred into a furnace at the same temperature. The sample was held at 1000 °C for 5 minutes to ensure thermal equilibration and then allowed to cool naturally inside the furnace to room temperature, without any forced or rapid cooling step. Following cooling, the samples were prepared for characterization (cutting, polishing, and surface finishing) according to the procedure described previously. These specimens are denoted in the text by the code "LS-1000"

To more accurately illustrate the thermal treatment process in the three defined pathways, the temperature changes over time for each pathway are presented in Figure 1. These graphs provide an overview of the differences in cooling and heating conditions for each pathway and offer a better understanding of the relationship between thermal parameters and the final characteristics of the samples.

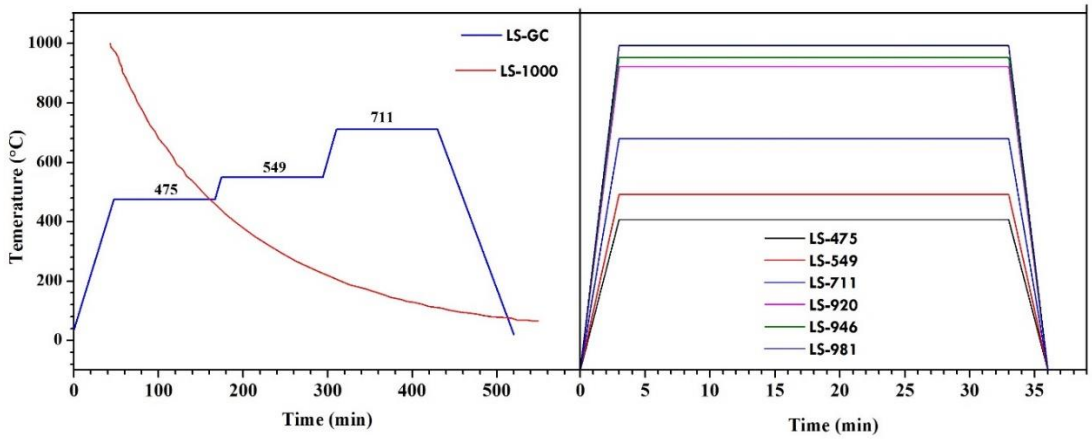


**Figure 1.** Specifications of the thermal treatment performed on lithium metasilicate ($Li_2SiO_3$) glass for phase evaluation using XRD testing. Method I: Non-isothermal heat treatment with very rapid heating to the temperatures specified in the DTA graph, holding for 30 minutes, and then rapid cooling to ambient temperature; Method II: Isothermal heat treatment at temperatures of 475°C, 549°C, and 711°C with a holding time of 120 minutes at each temperature and a heating rate of 10°C per minute; Method III: Quasi- isothermal heat treatment to simulate the glass cooling process during the infiltration process.





[ DOI: 10.22068/ijmse.4363 ]

## 2-2 Characterization Tests

To investigate the thermal behavior of lithium metasilicate ($Li_2SiO_3$) glass and to determine the glass transition temperature ($T_g$), nucleation temperature ($T_n$), crystallization temperature ($T_c$), and melting temperature ($T_m$), differential thermal analysis (DTA) was employed. For DTA analysis, amorphous glass powders previously ground in an agate mortar and sieved through a 100-mesh screen (<150 μm) were used to ensure uniform particle size and stable thermal response. DTA was performed on approximately 20 mg of glass powder, heated from room temperature to 1000 °C at a rate of 10 °C·min$^{-1}$ in alumina crucibles under air atmosphere. To determine the amorphous nature of the cast glass and to identify the phases formed during thermal treatment, X-ray diffraction (XRD) analysis was utilized. Prior to XRD testing, bulk specimens were manually ground in an agate mortar and sieved through a 200-mesh screen (<75 μm) to obtain homogeneous fine powders suitable for quantitative diffraction. XRD measurements were performed using a Philips PW3710 diffractometer operated at 30 kV and 40 mA, with Cu Kα radiation (λ = 1.5406 Å). Diffraction patterns were collected over a 2θ range of 5–80° at a scanning rate of 0.02°/s. Phase identification was carried out using XPert HighScore Plus 3.0.5 software. After phase identification, quantitative phase analysis was performed using the Rietveld refinement method, and the volume fraction of each phase was calculated using MAUD software. Rietveld refinement was carried out using a pseudo-Voigt peak profile and a fifth-order polynomial background function. Refinement proceeded sequentially through four parameter groups: (i) background and scale factors, (ii) basic phase parameters including lattice constants and zero-shift, (iii) microstructural parameters (crystallite size and microstrain, modeled isotropically), and (iv) structural parameters, which were constrained using standard CIF files. Preferred orientation





[ DOI: 10.22068/ijmse.4363 ]

effects were evaluated using the March–Dollase model when necessary. Refinement quality was assessed using standard reliability indices (Rp, Rwp, Rexp, and $\chi^2$), which confirmed satisfactory convergence and an adequate match between the observed and calculated diffraction profiles for all samples. In addition, Sig and Rw values were consistently reduced to near-unity (Sig < 1.5) and below 20%, ensuring the accuracy and stability of the refinement. The isotropic size–strain model was applied to estimate crystallite sizes. Because no dedicated instrumental standard was measured concurrently with the samples, these crystallite size values are interpreted as relative comparative indicators rather than absolute measurements. Nevertheless, all samples were analyzed under identical instrumental settings, ensuring that the observed differences in peak broadening reliably reflect the influence of thermal history on crystallization behavior. CIF structural files from the Crystallography Open Database (COD) were used for precise pattern processing, including COD-2003027 for lithium disilicate ($Li_2Si_2O_5$), COD-1572506 for lithium metasilicate ($Li_2SiO_3$), COD-9012821 for β-lithium orthophosphate (β-$Li_3PO_4$), COD-1011097 for β-quartz, COD-1010938 for β-cristobalite, and COD-9002380 for γ-spodumene (γ-$LiAlSi_2O_6$). Texture analysis of the lithium metasilicate ($Li_2SiO_3$) phase was also examined using March–Dollase functions within MAUD. Relative peak intensities were compared with reference CIF values to detect deviations from random orientation, and representative pole figure plots were generated to visualize the dominant crystal orientations and their possible influence on microstructural development. The morphology of the microstructure, as well as the size and distribution of the phases, was examined using a field emission scanning electron microscope (FESEM). The glass-ceramic samples were etched in a 2.5 vol.% HF solution for 30 s prior to FESEM observation. It is noteworthy that to prevent charging of the samples during imaging, all surfaces were coated with gold for 45 seconds prior to microstructural examination. For quantitative ImageJ measurements, multiple FESEM





[ DOI: 10.22068/ijmse.4363 ]

micrographs from different regions of each specimen were analyzed. Regions were selected based on uniform contrast, absence of imaging artifacts, and clear visibility of individual crystal boundaries to avoid area-specific bias.

## 3- Results and Discussion

### 3-1 Evaluation of Crystallization Behavior (DTA)

Figure 2 shows the DTA and DDTA curves of lithium metasilicate ($Li_2SiO_3$) glass powder. An endothermic inflection near 475 °C is evident on the DDTA trace, marking the glass transition temperature ($T_g$). Three exothermic peaks are observed at approximately 549°C, 711°C, and 920°C, which correspond to the crystallization of the respective phases. A relatively weak exothermic peak is observed at 549°C, which is low in intensity and only detectable in the DDTA graph. This peak is likely attributed to the crystallization of the lithium metasilicate phase ($Li_2SiO_3$). Part of this phase at higher temperatures (around 711°C) may transform into the lithium disilicate phase ($Li_2Si_2O_5$) [35]. The second peak, appearing at 711°C, has a high intensity and is likely associated with the crystallization of the lithium disilicate ($Li_2Si_2O_5$) phase [35]. The third peak, around 920°C, may result from the crystallization of silica phases such as cristobalite or quartz, or from increased order in the amorphous β-lithium orthophosphate (β-$Li_3PO_4$) phase [35, 37]. Additionally, two endothermic peaks are observed at 946°C and 981°C, which may relate to polymorphic transitions or the melting of crystalline phases present in the sample. For a more precise identification of the nature of the thermal peaks observed in the DTA test, X-ray diffraction (XRD) patterns corresponding to the thermally treated samples at the respective temperatures will be examined in the next section.





[ DOI: 10.22068/ijmse.4363 ]

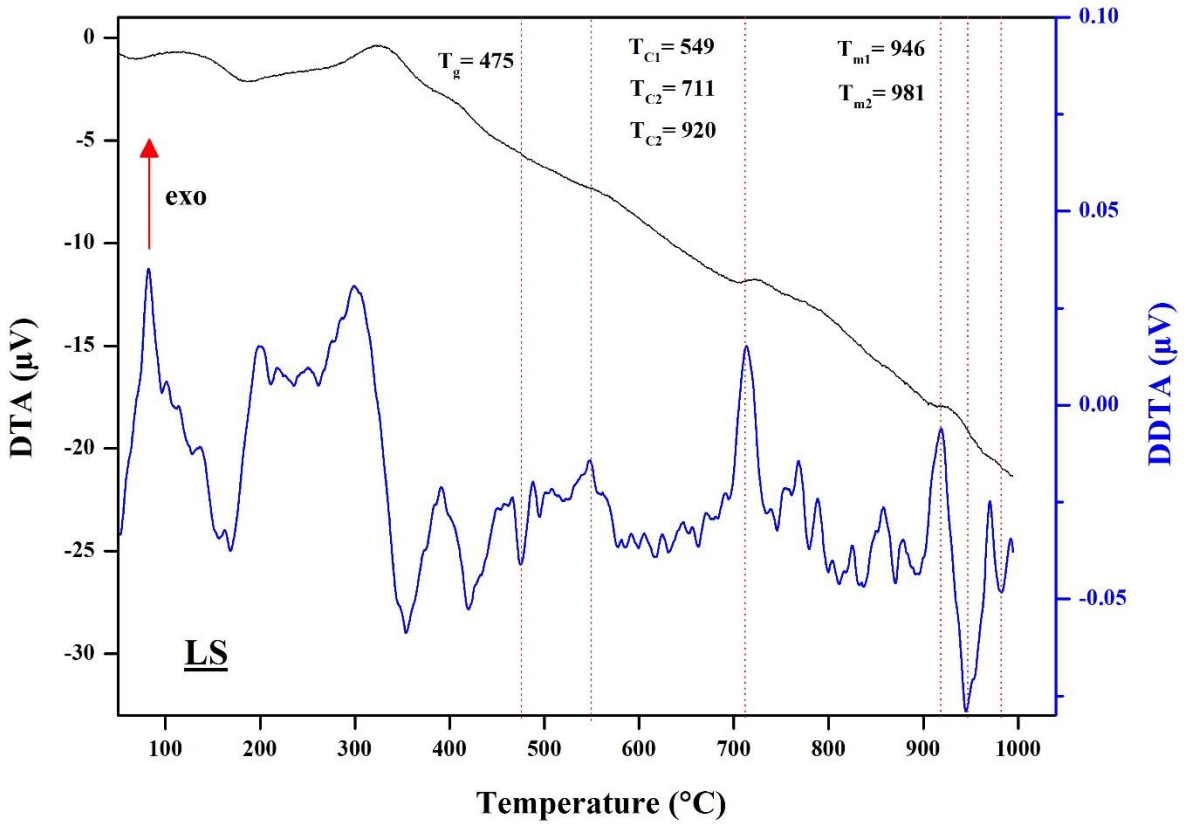


**Figure 2.** DTA and DDTA curves obtained from lithium metasilicate (LS) glass powder.

### 3-2 Evaluation of Crystalline Phases (XRD) and Determination of Phase Crystallization Percentages

lithium metasilicate ($Li_2SiO_3$) glass was subjected to X-ray diffraction (XRD) testing after thermal treatment at various temperatures. The resulting XRD patterns are presented in Figure 3, along with the phase analysis and quantification results in Table 1 and Figure 4. The identified phases include lithium metasilicate ($Li_2SiO_3$), lithium disilicate ($Li_2Si_2O_5$), β-lithium orthophosphate (β-$Li_3PO_4$), quartz ($SiO_2$), cristobalite ($SiO_2$), and γ-spodumene (γ-$LiAlSi_2O_6$).





[ DOI: 10.22068/ijmse.4363 ]

Based on Figure 3a, the initial lithium metasilicate ($Li_2SiO_3$) glass sample is completely amorphous and lacks any crystallization peaks. In the non-isothermal heat treatment, up to 475°C (corresponding to $T_g$), the structure remains amorphous (Figure 3b), with only a very small amount (0.8 wt.%) of the $Li_2SiO_3$ phase identified in the glassy matrix. Considering the typical detection limits of laboratory XRD (LOD ≈ 0.1–0.2 wt%), this fraction lies above the minimum detectable threshold and is therefore regarded as physically meaningful within the refinement accuracy. In the temperature range of 500–590°C, the presence of $P_2O_5$ leads to the formation of β-lithium orthophosphate (β-$Li_3PO_4$) nanophases. The high field strength $P^{5+}$ions facilitate the asymmetric separation of phosphates by absorbing O2- ions from the silica network, and subsequently, by absorbing $Li^+$ ions, the formation of β-lithium orthophosphate (β-$Li_3PO_4$) becomes possible according to Equations 1 and 2 [43]. This process creates lithium-rich areas around $Li_3PO_4$, providing nucleation sites for the crystallization of $Li_2SiO_3$ at temperatures of 520–590°C (Equations 3 and 4).

$$(Si-O^{\cdots}Li^{+})_{(glass)} + P_2O_{5(glass)} = 3(Si-O-Si)_{glass} + 2Li_3PO_{4(crystalline)} \quad \text{Equation (1)}$$

$$P_2O_{5(glass)} + 3Li_2O_{(glass)} = 2Li_3PO_{4(crystalline)} \quad \text{Equation (2)}$$

$$Li_2O_{(amorphous)} + Q^2{}_{(amorphous)} = Li_2SiO_{3(crystalline)} \quad \text{Equation (3)}$$

$$Li_2O_{(amorphous)} + Q^3{}_{(amorphous)} = Li_2SiO_{3(crystalline)} + Q^4{}_{(amorphous)} \quad \text{Equation (4)}$$

Thus, at 549°C, there is good compatibility between the XRD pattern (Figure 3c) and the reactions occurring in Equations 1 to 4. Although the $Li_3PO_4$ phase cannot be detected due to its amorphous nature, low crystallinity, nanometric size, or XRD detection limitations. Research findings indicate





[ DOI: 10.22068/ijmse.4363 ]

that the identification of phases such as $Li_3PO_4$ in glasses containing less than 3 mol% $P_2O_5$, which have been thermally treated at 450-550°C, is not feasible [44, 45].

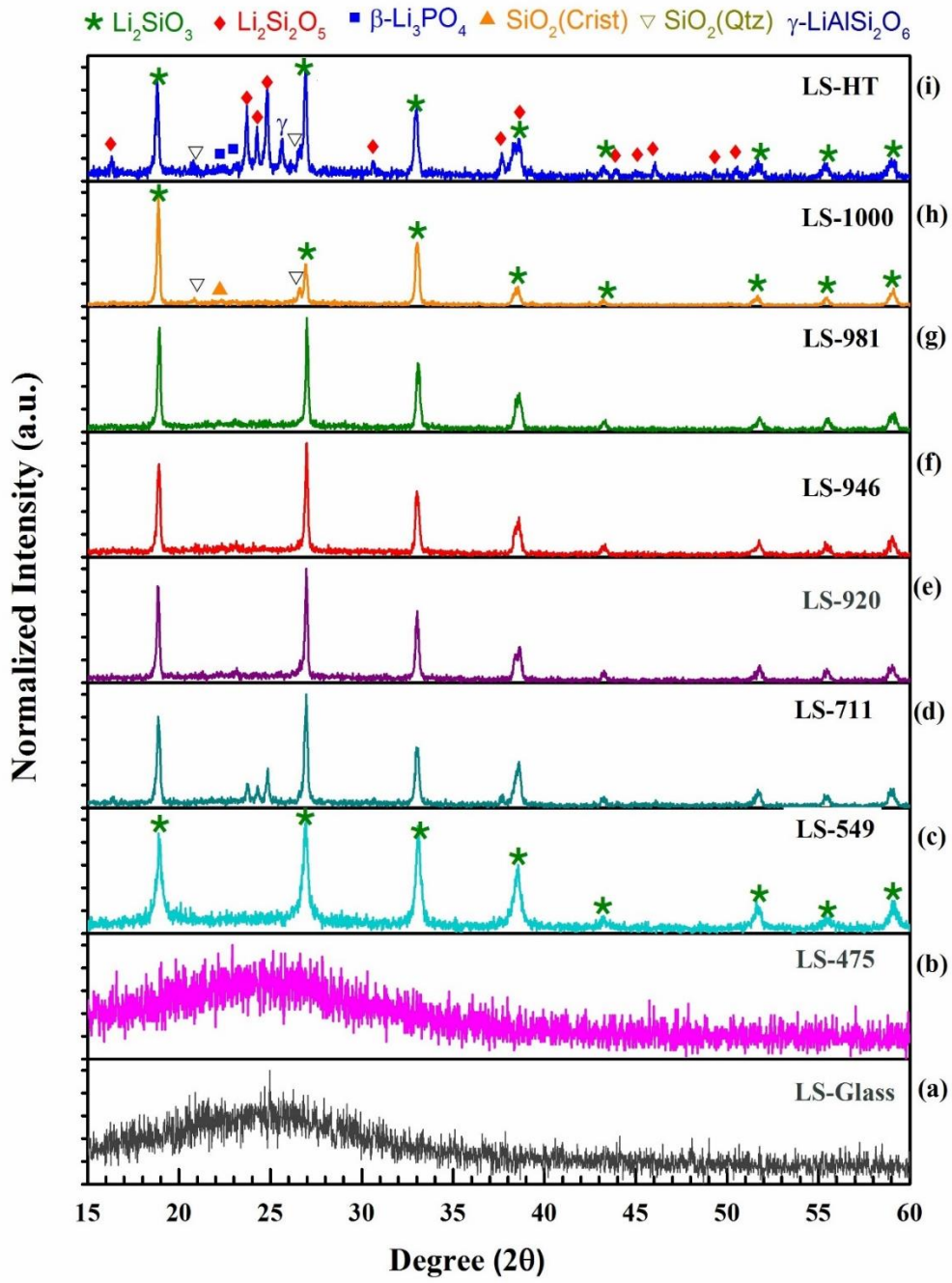


**Figure 3.** XRD patterns of lithium metasilicate glass after different thermal treatments at various temperatures.





[ DOI: 10.22068/ijmse.4363 ]

As the temperature increases from 549°C to 711°C, the phases of $Li_2Si_2O_5$, beta-quartz, and beta-cristobalite form alongside $Li_2SiO_3$. The transformation reaction of $Li_2SiO_3$ to $Li_2Si_2O_5$ occurs according to Equation 5 in the presence of glassy silica. At this temperature, $Li_2SiO_3$ is the dominant phase (65.7 wt.%), while $Li_2Si_2O_5$ (12.8 wt.%), beta-cristobalite (0.4 wt.%), and quartz (0.3 wt.%) are identified as secondary phases. Since the formation of $Li_2Si_2O_5$ requires higher activation energy compared to $Li_2SiO_3$, $Li_2SiO_3$ is initially formed during thermal treatment, and then $Li_2Si_2O_5$ appears through its transformation [41].

$$Li_2SiO_{3(crystal)} + SiO_{2(glass)} = Li_2Si_2O_{5(crystal)} \qquad \text{Equation (5)}$$

As the temperature rises to 920°C, the peaks of $Li_2Si_2O_5$ disappear, and weak peaks of $Li_3PO_4$ appear at 19.90° and 23.14° in 2θ. The absence of an endothermic event in the DTA and the observation of an exothermic peak at this temperature confirm the crystallization of $Li_3PO_4$. The disappearance of $Li_2Si_2O_5$ may be due to thermal decomposition or kinetic limitations in the non-isothermal treatment.

According to reports by Holland et al. [42], lithium disilicate melts around 950°C according to Reaction 6. However, in the DTA graph of the lithium metasilicate ($Li_2SiO_3$) glass powder (Figure 2), no endothermic event was observed around 920°C, and the existing peak is exothermic. This peak may be due to the crystallization of the β-lithium orthophosphate phase (β-$Li_3PO_4$), which also aligns with the XRD pattern; although the intensity of this phase's peak, like that of beta-cristobalite and beta-quartz, is weak at this temperature. The disappearance of lithium disilicate ($Li_2Si_2O_5$) at 920°C may relate to its thermal decomposition at high temperatures or the nature of





[ DOI: 10.22068/ijmse.4363 ]

the non-isothermal heat treatment, as the rapid increase in temperature to 920°C may hinder the kinetic formation of this phase.

$$Li_2Si_2O_{5(crystal)} = Li_2SiO_{3(crystal)} + SiO_{2(glass)} \quad \text{Equation (6)}$$

In general, crystallization behavior is influenced by the initial composition of the glass, the presence of nucleating agents, and stabilizing oxides (such as $Al_2O_3$, $B_2O_3$, CaO, ZnO, and $ZrO_2$). The molar ratio of $SiO_2/Li_2O$ plays an important role in phase stability; higher ratios above 2 facilitate the transformation of $Li_2SiO_3$ to $Li_2Si_2O_5$ [42], while ratios below 2 reduce the activation energy for the crystallization of $Li_2SiO_3$ and increase its stability at temperatures above 800°C [43]. In this study, the $SiO_2/Li_2O$ ratio is 1.31; therefore, lithium metasilicate ($Li_2SiO_3$) is expected to be the dominant and stable phase in the glass-ceramic. Additionally, the duration of thermal treatment also affects the process, where a short duration at an appropriate temperature can facilitate the growth and nucleation of this phase.

At 946°C, the phase composition is similar to that at 920°C, but the weight percentages of all phases have decreased, which may indicate a phase transition to an amorphous or molten state. The endothermic peak in the DTA at this temperature is likely related to the melting or simultaneous decomposition of $Li_2SiO_3$ and $Li_3PO_4$, with the two phases of $Li_2SiO_3$ and $Li_3PO_4$ decreasing from 58.1 wt.% and 1.2 wt.% at 920°C to 49.9 wt.% and 0.9 wt.% at 946°C, respectively.

At 981°C, $Li_3PO_4$ and cristobalite are eliminated, and $Li_2SiO_3$ decreases to 38.1 wt.%. Therefore, the endothermic peak in the DTA at this temperature may be attributed to the complete melting of





[ DOI: 10.22068/ijmse.4363 ]

$Li_3PO_4$, partial melting of $Li_2SiO_3$, or the endothermic transformation of cristobalite to quartz [44]. Based on the DTA curve and the X-ray diffraction (XRD) pattern of lithium metasilicate ($Li_2SiO_3$) glass, it is predicted that the lithium metasilicate ($Li_2SiO_3$) phase along with two other phases will melt at temperatures above 1000°C.

The results of isothermal heat treatment (LS-1000) indicate that during cooling from the melt to room temperature, four phases $Li_2SiO_3$ (84.7± 0.9 wt.%), $Li_3PO_4$ (1.4± 0.3 wt.%), quartz (0.6± 0.1 wt.%), and cristobalite (0.3± 0.1 wt.%) are formed. The crystallization mechanism is similar to that of non-isothermal treatment, but the high stability of $Li_2SiO_3$ prevents the formation of $Li_2Si_2O_5$.

It is expected that the common reactions in lithium metasilicate ($Li_2SiO_3$) glasses during non-isothermal heat treatment will also occur in this process. According to Figure 5, at temperatures above 1201°C and within a range of approximately 63 wt.% $SiO_2$, the only present phase is the molten phase. This diagram is plotted for the binary system $Li_2O$–$SiO_2$ and shows that upon cooling from 1201°C to 1024°C, the lithium metasilicate ($Li_2SiO_3$) phase forms within the melt. However, in lithium metasilicate ($Li_2SiO_3$) glasses containing oxides such as $P_2O_5$ and $Al_2O_3$, the crystallization of phases is somewhat different. In such systems, as the temperature decreases from the molten state, $P_2O_5$ initially reacts with $Li_2O$ to form β-lithium orthophosphate (β-$Li_3PO_4$) nuclei (Equation 2). During non-isothermal heat treatment, due to the lack of precise control over the cooling rate, these nuclei grow through the Ostwald ripening process, reducing their density [45]. Then, with further temperature reduction and the creation of silica-rich regions, the lithium metasilicate ($Li_2SiO_3$) phase precipitates on the β-lithium orthophosphate (β-$Li_3PO_4$) nuclei. As seen in the XRD pattern in Figure 3, alongside the formation of lithium metasilicate ($Li_2SiO_3$), the phases of beta-quartz and beta-cristobalite are also created. Since in non-isothermal heat treatment, the lithium metasilicate ($Li_2SiO_3$) phase is stable in this system and the lithium disilicate ($Li_2Si_2O_5$)





[ DOI: 10.22068/ijmse.4363 ]

phase completely disappears as the temperature increases from 711°C to 920°C, it is expected that in the LS-1000 sample during cooling from the molten state to lower temperatures, lithium metasilicate ($Li_2SiO_3$) will remain stable. As observed, the XRD results also confirm this.

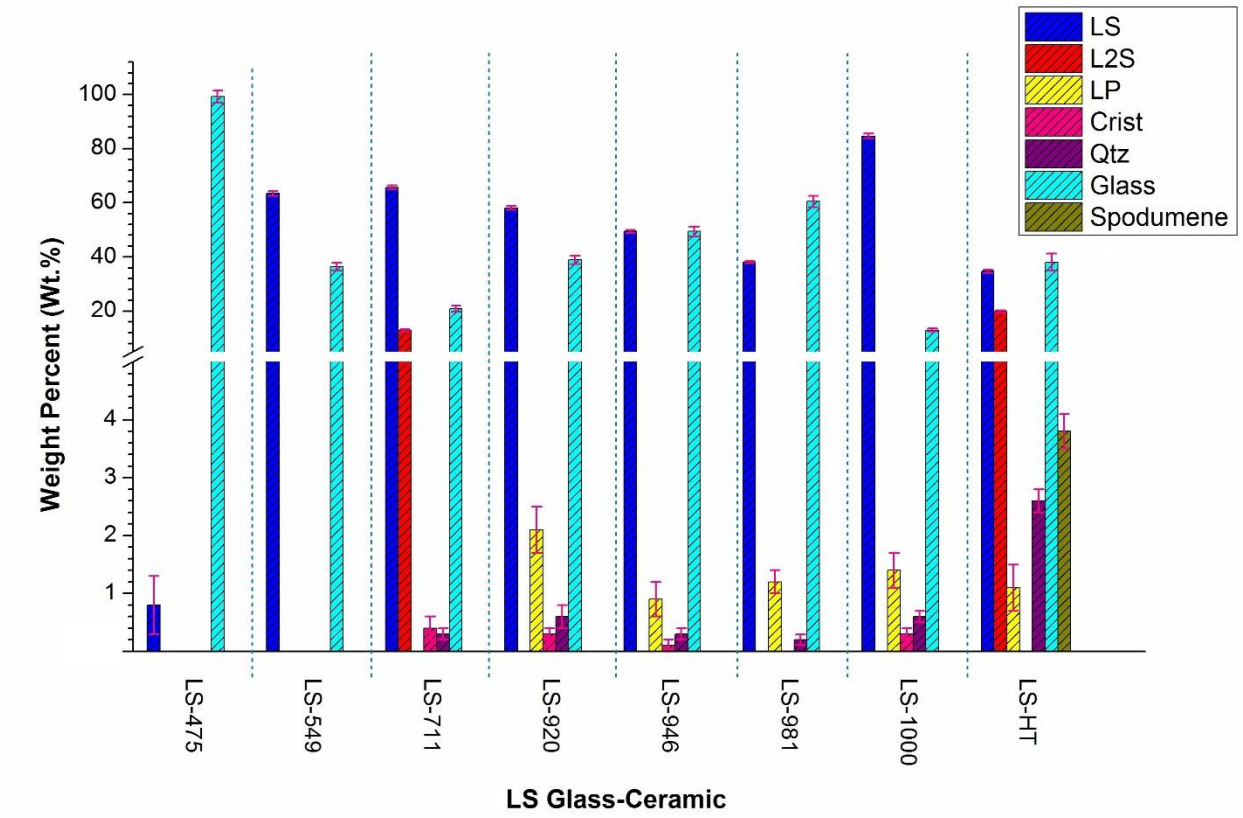


**Figure 4.** Quantification of crystalline phases in thermally treated lithium metasilicate ($Li_2SiO_3$) glass-ceramic under various conditions and the corresponding residual glass phase.

A comparison of the diffraction patterns and their quantified results (Figures 3 and 4) indicates that thermal treatment conditions play a significant role in the percentage and type of formed phases. In the isothermal process (LS-HT), the crystallization percentage (62±0.9 wt.%) is lower than that of LS-1000 (87±1 wt.%), but the variety of formed phases is greater: (34.7± 0.5 wt.%) $Li_2SiO_3$, (19.8±0.4 wt.%) $Li_2Si_2O_5$, γ-spodumene (γ-$LiAlSi_2O_6$) (3.8±0.3 wt.%), quartz (2.6±0.2 wt.%), and (1.1±0.4 wt.%) $Li_3PO_4$. The difference in crystallization percentage and phase composition is related to the thermal treatment conditions and the mechanisms of nucleation and





[ DOI: 10.22068/ijmse.4363 ]

crystal growth. In LS-1000, due to slow cooling and a thermal gradient, sufficient time for nucleation and crystal growth is likely provided, resulting in a higher crystallization percentage [51, 52]. In contrast, LS-HT, which undergoes controlled thermal treatment at nucleation and crystal growth temperatures, kinetically allows for the crystallization of equilibrium phases; however, due to the short nucleation and growth time, there may not be enough opportunity for the glass phase to convert into crystalline phases, leading to a lower crystallization percentage [53]. The nucleation process is crucial in determining the crystallized phases. Depending on the processing conditions, different crystals may exhibit bulk or surface crystallization. Lodesani et al. [54] concluded in their studies that lithium disilicate ($Li_2Si_2O_5$) and β-lithium orthophosphate (β-$Li_3PO_4$) crystallize volumetrically within the glass, while lithium metasilicate ($Li_2SiO_3$) forms on the surface of the glass. Therefore, the continuous cooling of LS-1000 in the furnace and the presence of a temperature gradient increase the likelihood of surface crystallization in the sample, resulting in a higher ratio of the lithium metasilicate ($Li_2SiO_3$) phase. Phosphorus oxide is widely recognized as an effective nucleating agent in this glass system, promoting the formation of β-lithium orthophosphate (β-$Li_3PO_4$), which subsequently facilitates the crystallization of lithium metasilicate ($Li_2SiO_3$) and lithium disilicate ($Li_2Si_2O_5$) [47]. The LS-1000 sample may provide better conditions for the performance of phosphorus oxide and consequently for the nucleation and crystallization of β-lithium orthophosphate (β-$Li_3PO_4$) due to the nature of its thermal treatment process, resulting in higher crystallization. In contrast, in the LS-HT thermal treatment, the formation of β-lithium orthophosphate (β-$Li_3PO_4$) with low-range order at low temperatures may have prevented the full utilization of the nucleation potential of phosphorus oxide.





[ DOI: 10.22068/ijmse.4363 ]

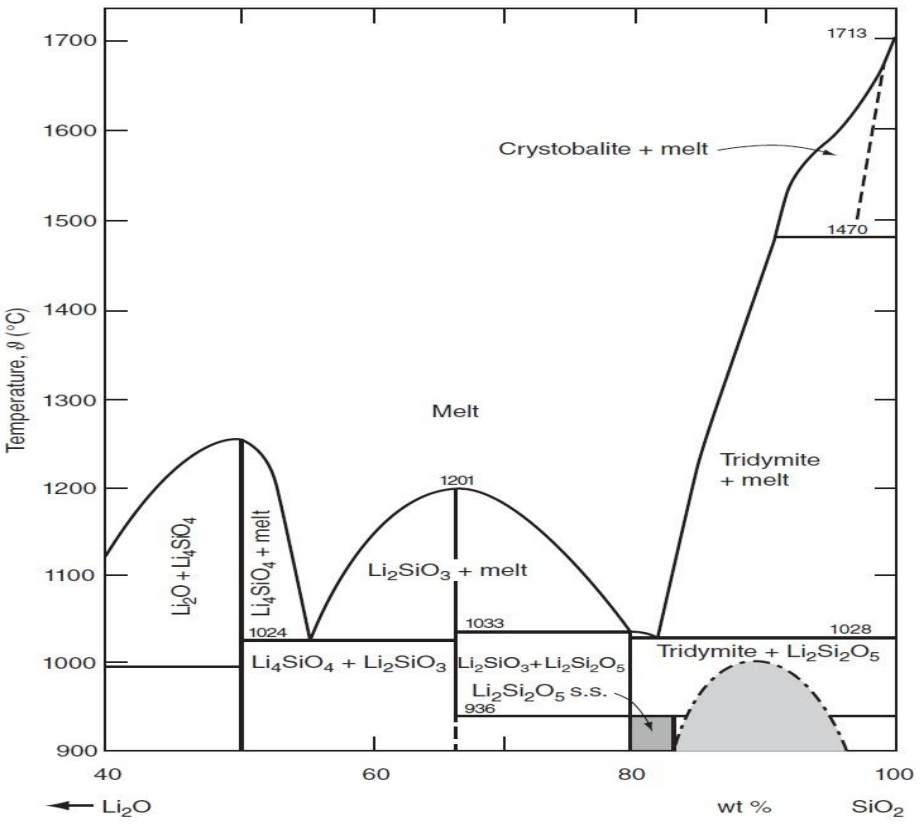


**Figure 5.** A part of the phase diagram of the $SiO_2$–$Li_2O$ binary system [50].

As seen in Table 1, lithium disilicate ($Li_2Si_2O_5$) and γ-spodumene (γ-$LiAlSi_2O_6$) phases were not detected in the LS-1000 glass-ceramic under the present XRD conditions, unlike in LS-HT. Given the detection limits of XRD, the presence of trace or nanoscale domains of these phases cannot be fully ruled out. The thermal treatment conditions, particularly the continuous cooling from the molten state, did not provide the thermodynamic and kinetic requirements necessary for the formation of l lithium disilicate ($Li_2Si_2O_5$) and γ-spodumene (γ-$LiAlSi_2O_6$). It is also possible that these phases were re-dissolved in the melt during the slow cooling process. Overall, differences in cooling rates, thermal treatment stages, and the role of nucleating agents are key factors determining the amount and type of crystallization, leading to the observed differences in phases and crystallization percentages between the two samples.





[ DOI: 10.22068/ijmse.4363 ]

Figure 6 shows a comparison of the XRD patterns of the two glass-ceramics, LS-1000 and LS-HT. As observed, the intensity of the diffraction peaks corresponding to the lithium metasilicate ($Li_2SiO_3$) phase in LS-1000, including the (020), (130), (111), (110), (002), and (210) planes, is significantly higher than that in LS-HT. This increased intensity can be attributed to the higher crystallization percentage (87±1 wt.% versus 62±0.9 wt.%), larger crystal sizes (337 nm compared to 147 nm), and greater crystalline order. The shorter peaks in LS-HT indicate the presence of smaller crystals or a higher proportion of the amorphous phase.

Since the intensity of diffraction peaks depends on the size and order of the crystals, the growth of larger crystals in LS-1000, resulting from the nature of its thermal treatment and slow cooling, accounts for this difference. Although thermal gradients and variable cooling rates can promote preferential growth or orientation, microstructural texture analysis using Maud software revealed no preferred orientation in these crystals, and their distribution in the glassy matrix is entirely random.

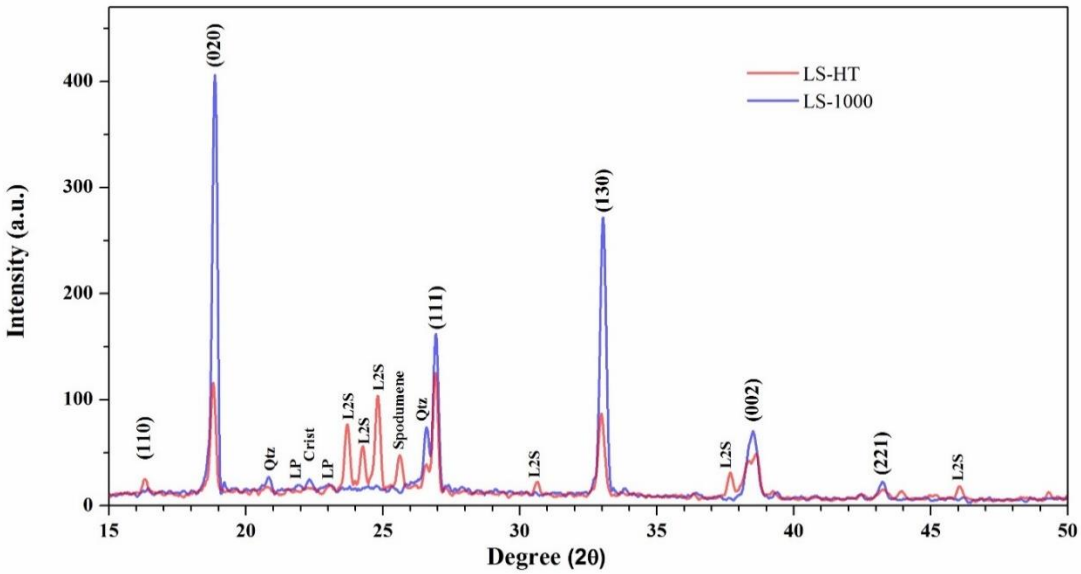


**Figure 6.** Comparison of the XRD pattern of lithium metasilicate ($Li_2SiO_3$) glass-ceramics LS-1000 and LS-HT.





[ DOI: 10.22068/ijmse.4363 ]

**Table 1.** Crystalline phases crystallized and the crystallization percentage of lithium metasilicate ($Li_2SiO_3$) glass-ceramics.

| Sample | Crystalline Phases (wt. %) | Crystallinity (Wt. %) | Residual Glass Content (Wt. %) |
|---|---|---|---|
| LS-475 | 0.8± 0.5 $Li_2SiO_3$ | 0.8±0.5 | 99.2±2.3 |
| LS-549 | 63.4± 0.8 $Li_2SiO_3$ | 63.4±0.8 | 36.6±1.4 |
| LS-711 | 65.7± 0.7 $Li_2SiO_3$ – 12.8± 0.4 $Li_2Si_2O_5$ – 0.3± 0.1 β-Qtz – 0.4± 0.2 β-Crist | 79.2±0.8 | 20.8±1.1 |
| LS-920 | 58.1± 0.7 $Li_2SiO_3$ – 0.6± 0.2 β-Qtz – 0.3± 0.1 β-Crist –2.1± 0.4 β-$Li_3PO_4$ | 61.1±0.8 | 38.9±1.6 |
| LS-946 | 49.4± 0.6 $Li_2SiO_3$ – 0.3± 0.1 β-Qtz – 0.1± 0.1 β-Crist –0.9± 0.3 β-$Li_3PO_4$ | 50.7±0.7 | 49.3±1.8 |
| LS-981 | 38.1± 0.4 $Li_2SiO_3$ – 0.2± 0.1 β-Qtz –1.2± 0.2 β-$Li_3PO_4$ | 39.5±0.5 | 60.5±0.6 |
| LS-1000 | 84.7± 0.9 $Li_2SiO_3$ – 0.6± 0.1 β-Qtz – 0.3± 0.1 β-Crist –1.4± 0.3 β-$Li_3PO_4$ | 87±1 | 13±0.6 |
| LS-HT | 34.7± 0.5 $Li_2SiO_3$ – 19.8± 0.4 $Li_2Si_2O_5$ – 3.8± 0.3 γ-$LiAlSi_2O_6$ – 2.6± 0.2 β-Qtz–1.1± 0.4 β-$Li_3PO_4$ | 62±0.9 | 38±3.2 |

### 3-3 Microstructure Evaluation (FESEM)

Figure 7 shows the microstructure of lithium metasilicate ($Li_2SiO_3$) glass-ceramics after polishing and etching in a 2.5% volumetric solution of hydrofluoric acid for 30 seconds. In the sample subjected to controlled thermal treatment (LS-HT) (Figures 7a to b), a combination of plate/strip-like and rod-like morphologies is observed. According to the studies by Daguan et al. [37] and Suárez et al. [35], the plate or strip morphologies are related to the crystallized lithium metasilicate ($Li_2SiO_3$) phase. As previously stated, the phase analysis results confirm the presence of two main phases, namely lithium metasilicate ($Li_2SiO_3$) and lithium disilicate ($Li_2Si_2O_5$), in the LS-HT





[ DOI: 10.22068/ijmse.4363 ]

sample. Therefore, the rod-like structures observed in this sample likely belong to the lithium disilicate ($Li_2Si_2O_5$) phase.

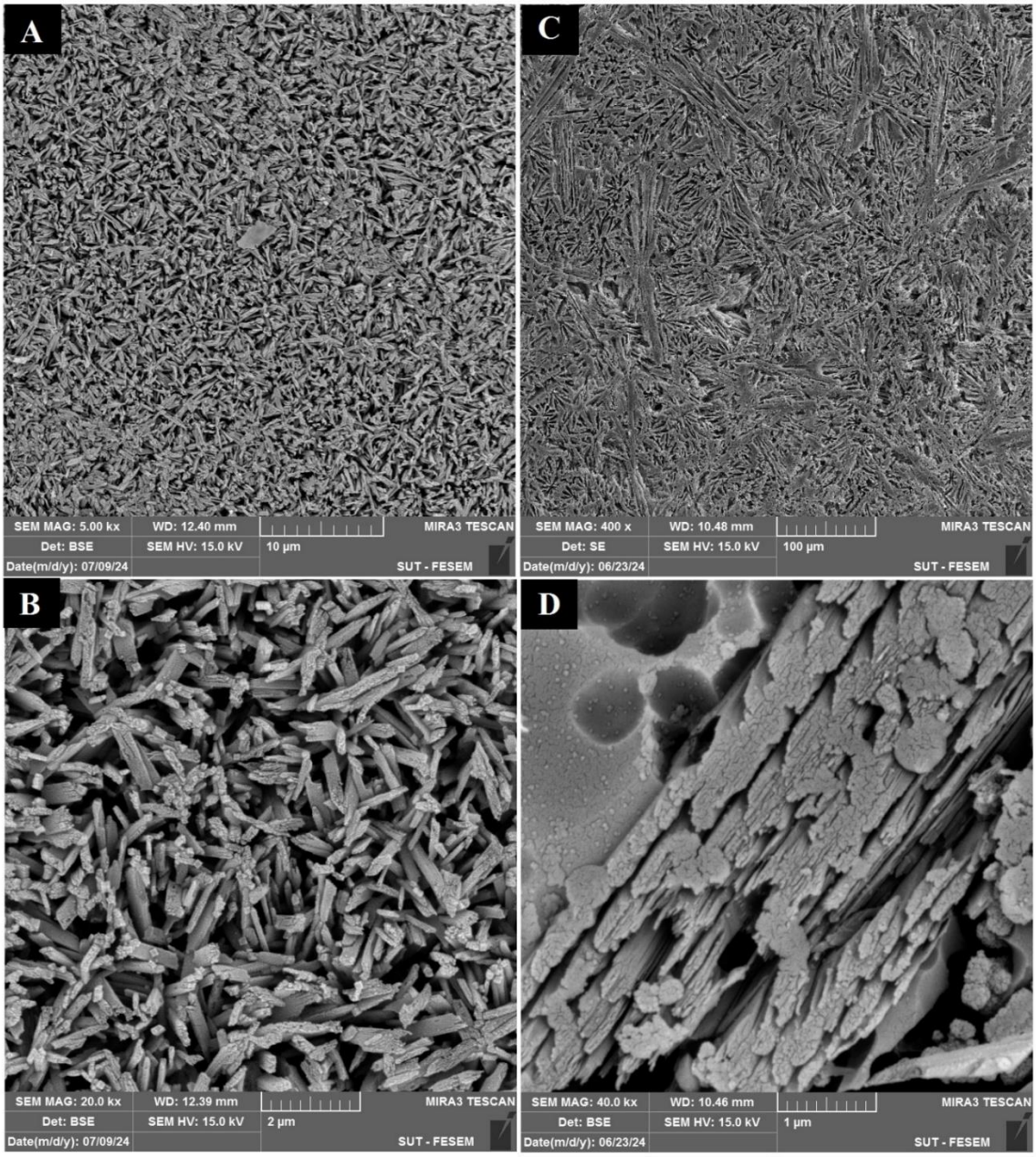


**Figure 7.** FESEM micrographs of lithium metasilicate ($Li_2SiO_3$) glass-ceramics: (a–b) correspond to the LS-HT sample (controlled thermal treatment), and (c–d) correspond to the LS-1000 sample (quasi-isothermal cooling).





[ DOI: 10.22068/ijmse.4363 ]

In contrast, the sample subjected to uncontrolled thermal treatment (LS-1000) is primarily composed of interlocked strip-like crystals (Figures 7c to d). In Figures 7c and 7d, the aggregation of several plate-like crystals leads to the formation of colonies with a striped appearance. Additionally, Figure 7d clearly shows the presence of spherical voids resulting from the removal of the β-lithium orthophosphate (β-$Li_3PO_4$) phase due to chemical etching.

Quantitative analysis results using ImageJ software indicate that the controlled thermal treatment in LS-HT leads to the formation of a microstructure with smaller, more uniform crystals, exhibiting a more balanced geometry and a random distribution in the glassy matrix. In contrast, the uncontrolled thermal treatment in LS-1000, due to thermal gradients and lack of control over the cooling rate, significantly increases the dimensions of the crystals and their length-to-thickness ratio, resulting in a coarse structure that is potentially prone to a decline in mechanical properties. The quantitative values related to the length, thickness, and length-to-thickness ratio of lithium metasilicate ($Li_2SiO_3$) crystals under the two thermal conditions are presented in Table 2. These results demonstrate that thermal parameters strongly influence the crystallization pathway and final microstructure of lithium metasilicate ($Li_2SiO_3$) glass-ceramics. The LS-HT sample exhibited a more uniform microstructure with smaller and well-distributed crystals, whereas the LS-1000 sample showed a coarser and more heterogeneous morphology. While such microstructural distinctions are known to affect the functional and mechanical behavior of silicate-based glass-ceramics, the present study is limited to structural evaluation, and quantitative mechanical characterization will be addressed in future work. It should also be clarified that the crystalline phases discussed here are not present during the infiltration stage itself, since the glass is fully molten and exists as a single-phase liquid at infiltration temperatures. Their significance emerges only during post-infiltration cooling, where the type, morphology, and thermal expansion





[ DOI: 10.22068/ijmse.4363 ]

behavior of the crystallized phases can influence residual stresses, interfacial bonding, and the long-term stability of the glass–zirconia composite. Accordingly, the phase assemblages reported in this study reflect the behavior of the glass during cooling under simulated thermal histories rather than during infiltration itself. While the present work focuses solely on structural features, it is also important to clarify the scope of the LS-1000 pathway. The LS-1000 pathway represents only a thermal simulation of slow furnace cooling and does not reproduce actual glass infiltration, capillary flow, wetting, or interfacial reactions with zirconia. Therefore, the results presented here describe the crystallization behavior under simulated thermal conditions, and future studies should include direct infiltration experiments on porous zirconia to validate structural and interfacial responses under real processing conditions.

**Table 2.** Quantitative comparison of the microstructural characteristics of lithium metasilicate ($Li_2SiO_3$) crystals under two different thermal conditions.

| Microstructural Feature | LS-HT | LS-1000 | Growth Ratio (LS-1000/LS-HT) |
|---|---|---|---|
| Average crystal length (μm) | 5.2±0.37 | 54.1±19.2 | 10.4±0.37 |
| Average crystal thickness (μm) | 0.17±0.03 | 5.3±1.2 | 31.2±9 |
| Aspect ratio (Length/Thickness) | 30.6±5.8 | 10.2±4.3 | 0.3±0.17 |

## 4- Conclusion

The findings of this study indicate that the thermal path applied during the crystallization process of lithium metasilicate ($Li_2SiO_3$) glass plays a decisive role in its phase transformation and final microstructure. Under controlled isothermal heat treatment conditions, multiple phases, including $Li_2SiO_3$ and $Li_2Si_2O_5$, were formed with an overall crystallization percentage of about 62±0.9%, resulting in a uniform microstructure with fine grains that may enhance mechanical properties. In contrast, the simulated thermal treatment for infiltration (LS-1000) resulted in a higher





[ DOI: 10.22068/ijmse.4363 ]

crystallization percentage of about 87±1% and the predominance of the lithium metasilicate ($Li_2SiO_3$) phase, with no formation of lithium disilicate ($Li_2Si_2O_5$), but created a coarse and nearly heterogeneous structure that likely has lower mechanical strength. Therefore, the precise selection and control of the thermal path are essential in designing suitable materials for infiltration. This study serves as a first step, providing a deeper understanding of the relationship between thermal path and the microstructure of lithium metasilicate ($Li_2SiO_3$) glass in the absence of a zirconia framework, laying a scientific foundation for the development of optimized processes. Furthermore, a direct investigation of the infiltration of this glass into porous zirconia and the assessment of the effect of operational conditions on adhesion, aesthetics, and the strength of the final composite could pave the way for developing durable and high-performance dental restorations. Finally, for the practical application of lithium metasilicate ($Li_2SiO_3$) in all-ceramic restorations, future research should focus on optimizing thermal cycles according to actual infiltration conditions and conducting a comprehensive study of the mechanical and optical properties of the material. Future work will focus on quantifying mechanical and functional properties to establish comprehensive structure–property correlations.





[ DOI: 10.22068/ijmse.4363 ]

## References

[1] M.B. Blatz, G. Chiche, O. Bahat, R. Roblee, C. Coachman, H.O. Heymann, Evolution of aesthetic dentistry, Journal of Dental Research 98(12) (2019) 1294-1304.

[2] A. Limones, P. Molinero-Mourelle, L. Azevedo, M. Romeo-Rubio, A. Correia, M. Gómez-Polo, Zirconia-ceramic versus metal-ceramic posterior multiunit tooth-supported fixed dental prostheses: A systematic review and meta-analysis of randomized controlled trials, The Journal of the American Dental Association 151(4) (2020) 230-238.e7.

[3] Y. Zhang ,G. Wang, T. Kong, S. Yao, J. Wu, Infiltrating fluorapatite glass-ceramics on the surface of dental 3% yttria-stabilized zirconia to enhance bond strength, Surface and Coatings Technology 461 (2023) 129436.

[4] Z. Shamohammadi Gahsareh, S. Banijamali, A. Aghaei, Preparation and characterization of $P_2O_5$ containing canasite glass-ceramics as potential materials for dental restorations, Iranian Journal of Materials and Engineering 20(2) (2023) 1-17.

[5] B. Stawarczyk, C. Keul, M. Eichberger, D. Figge, D. Edelhoff, N. Lümkemann, Three generations of zirconia: From veneered to monolithic. Part I, Quintessence international 48(5) (2017).

[6] B. Stawarczyk, C. Keul, M. Eichberger, D. Figge, D. Edelhoff, N. Lümkemann, Three generations of zirconia: From veneered to monolithic. Part II, Quintessence International 48(6) (2017).

[7] N. Kolakarnprasert, M.R. Kaizer, D.K. Kim ,Y. Zhang, New multi-layered zirconias: Composition, microstructure and translucency, Dental Materials 35(5) (2019) 797-806.





[ DOI: 10.22068/ijmse.4363 ]

[8] Y. Zhang, B.R. Lawn, Novel Zirconia Materials in Dentistry, Journal of Dental Research 97(2) (2017) 140-147.

[9] B. Huang, M .Chen, J. Wang, X. Zhang, Advances in zirconia-based dental materials: Properties, classification, applications, and future prospects, Journal of Dentistry 147 (2024) 105111.

[10] N. Rahbar, W.O. Soboyejo, Design of functionally graded dental multilayers ,Fatigue & Fracture of Engineering Materials & Structures 34(11) (2011) 887-897.

[11] C. Cui, J. Sun, Optimizing the design of bio-inspired functionally graded material (FGM) layer in all-ceramic dental restorations, Dental Materials Journal 33(2) (2014) 173-178.

[12] J. Du, X. Niu, N. Rahbar, W. Soboyejo, Bio-inspired dental multilayers: Effects of layer architecture on the contact-induced deformation, Acta Biomaterialia 9(2) (2013) 5273-5279.

[13] S. Suresh, Graded Materials for Resistance to Contact Deformation and Damage, Science 292(5526) (2001) 2447-2451.

[14] H. Qian, C. Cui, T. Su, F. Zhang, J. Sun, Exploring the optimal pre-sintering temperature on compressive strength and anti-fatigue property of graded zirconia-based glass/zirconia structure, Dental Materials Journal 35(3) (2016) 341-344.

[15] P. Uasuwan, N. Juntavee, A. Juntavee, Flexural strength of novel glass infiltrated monochrome and multilayer high yttrium oxide containing zirconia upon various sintered cooling rates, Journal of Prosthodontics 33(S1) (2024) 47-59.

[16] Y. Zhang, L. Ma, Optimization of ceramic strength using elastic gradients, Acta Materialia 57(9) (2009) 2721-2729.





[ DOI: 10.22068/ijmse.4363 ]

[17]R.F. Villefort, M. Amaral, G.K.R. Pereira, T.M.B. Campos, Y. Zhang, M.A. Bottino, L.F. Valandro, R.M.J.D.M. de Melo, Effects of two grading techniques of zirconia material on the fatigue limit of full-contour 3-unit fixed dental prostheses, 33(4) (2017) e155-e164.

[18] Y. Zhang, J.W. Kim, Graded structures for damage resistant and aesthetic all-ceramic restorations, Dent Mater 25(6) (2009) 781-90.

[19] Y. Zhang, Overview: Damage resistance of graded ceramic restorative materials, Journal of the European Ceramic Society 32(11) (2012) 2623-2632.

[20] T.P.T. Nguyen, G.J. Oh, H.P. Lim, K.D. Yun, J.W. Kim, V.T .Vu, C. Park, J.S. Ban, H.S. Yang, S.W.J.J.o.N. Park, Nanotechnology, Evaluation of sandblasting on mechanical properties and cell response of bioactive glass infiltrated zirconia, 17(4) (2017) 2740-2742.

[21] M. Zhou, X. Zhang, Y. Zhang, D. Li, Z. Zhao ,X. Lyu, Q. Wang, K. Tang, Y. Jia, L. Niu, Investigation of the structure and mechanical properties of a novel dental graded glass/zirconia ceramic, Journal of the European Ceramic Society 43(13) (2023) 5671-5681.

[22] K. Mohit, T.A. Lakha, A. Chinchwade ,Q.A. Batul, M. Shaikh, S.M. Kheur, Effects of surface modification techniques on zirconia substrates and their effect on bonding to dual cure resin cement-An in-vitro study, The Journal of Indian Prosthodontic Society 22(2) (2022) 179-187.

[23] R. Amaral ,M. Özcan, M.A. Bottino, L.F. Valandro, Microtensile bond strength of a resin cement to glass infiltrated zirconia-reinforced ceramic: the effect of surface conditioning, Dental Materials 22(3) (2006) 283-290.





[ DOI: 10.22068/ijmse.4363 ]

[24]Z. Yan, J. Li, J. Chen, Z. Zhao, F. Li ,L. Zhang, J. Chen, F. Wang, Enhancing the bonding of zirconia to resin by constructing a graded zirconia-glass composite surface, Surfaces and Interfaces 64 (2025) 106374.

[25] M. Kaizer, S. Bano, M. Borba, V. Garg, M. Dos Santos, Y. Zhang, Wear behavior of graded glass/zirconia crowns and their antagonists, Journal of dental research 98(4) (2019) 437-442.

[26] N.M. Alfrisany, E. Somogyi-Ganss, L.E. Tam, B.D. Hatton, R.N. Sodhi, L. Yin, G.M. De Souza, Silica infiltration as a strategy to overcome zirconia degradation, Journal of Materials Science: Materials in Engineering 19(1) (2024) 30.

[27] M. Guazzato, M. Albakry, L. Quach, M.V. Swain, Influence of grinding, sandblasting, polishing and heat treatment on the flexural strength of a glass-infiltrated alumina-reinforced dental ceramic, Biomaterials 25(11) (2004) 2153-2160.

[28] X.-J. Sheng, H. Xu, Z.-H. Jin, Y.-L. Wang, Preparation of glass-infiltrated 3Y-TZP/$Al_2O_3$/glass composites, Materials Letters 58(11) (2004) 1750-1753.

[29] J.M. Tian, Y.L. Zhang, S.X. Zhang, X.P. Luo, Mechanical properties and microstructure of alumina-glass composites, Journal of the American Ceramic Society 82(6) (1999) 1592-1594.

[30] W.D. Wolf, K.J. Vaidya, L.F. Francis, Mechanical properties and failure analysis of alumina-glass dental composites, Journal of the American Ceramic Society 79(7) (1996) 1769-1776.

[31] P. Bajpai, P. Bhargava, Effect of heat treatment schedules and glass powder particle size on glass infiltration in porous alumina preforms, International Journal of Applied Ceramic Technology 11(3) (2014) 543-549.

[32] Y. Zhang, M.-j. Sun, D. Zhang, Designing functionally graded materials with superior load-bearing properties, Acta Biomaterialia 8(3) (2012) 1101-1108.





[ DOI: 10.22068/ijmse.4363 ]

[33] L. Mao, M.R. Kaizer, M. Zhao, B. Guo, Y.F. Song, Y. Zhang, Graded ultra-translucent zirconia (5Y-PSZ) for strength and functionalities, Journal of Dental Research 97(11) (2018) 1222-1228.

[34] A.C. da Silva, A.d.O.P. Ribeiro, L.M.M. Alves, F. de Camargo Ribeiro, T.B. Campos, R.M. de Melo Marinho, Zirconia gradation and thermal expansion compatibility between infiltration glass and antimicrobial glass, Ceramics International 48(14) (2022) 19746-19756.

[35] V.O. Soares, F.C. Serbena, I. Mathias, M.C. Crovace, E.D. Zanotto, New, tough and strong lithium metasilicate dental glass-ceramic, Ceramics International 47(2) (2021) 2793-2801.

[36] L.D. Silva, V.O. Soares, O. Peitl Filho, F.C. Serbena, M. Rampf, C. Ritzberger, M. Dittmer, E.D. Zanotto, Exploring new machinable, strong lithium metasilicate-based glass-ceramics for dental applications, Ceramics International 50(17) (2024) 31335-31344.

[37] J.K. Daguano, L. Dantas, V.O. Soares, M.F. Alves, C. Dos Santos, E.D. Zanotto, Optimizing the microstructure of a new machinable bioactive glass-ceramic, Journal of the Mechanical Behavior of Biomedical Materials 122 (2021) 104695.

[38] B.G. Simba, M.V. Ribeiro, P.A. Suzuki, M.F.R. Alves, K. Strecker, C. Dos Santos, Mechanical properties of lithium metasilicate after short-term thermal treatments, Journal of the Mechanical Behavior of Biomedical Materials 98 (2019) 179-186.

[39] S. Huang, P. Cao, Y. Li, Z. Huang, W. Gao, Nucleation and crystallization kinetics of a multicomponent lithium disilicate glass by in situ and real-time synchrotron X-ray diffraction, Crystal growth & design 13(9) (2013) 4031-4038.

[40] Y. Iqbal, W. Lee, D. Holland, P. James, Crystal nucleation in $P_2O_5$-doped lithium disilicate glasses, Journal of materials science 34 (1999) 4399-4411.







[ DOI: 10.22068/ijmse.4363 ]

[41] S. Huang, Z. Huang, W. Gao, P. Cao, In situ high-temperature crystallographic evolution of a nonstoichiometric $Li_2O.2SiO_2$ glass, Inorganic chemistry 52(24) (2013) 14188-14195.

[42] W. Höland, E. Apel, C. van't Hoen, V. Rheinberger, Studies of crystal phase formations in high-strength lithium disilicate glass–ceramics, Journal of Non-Crystalline Solids 352(38-39) (2006) 4041-4050.

[43] A. Gaddam, H.R. Fernandes, D.U. Tulyaganov, M.J. Ribeiro, J.M. Ferreira, The roles of $P_2O_5$ and $SiO_2/Li_2O$ ratio on the network structure and crystallization kinetics of non-stoichiometric lithium disilicate based glasses, Journal of Non-Crystalline Solids 481 (2018) 512-521.

[44] V. Swamy, S.K. Saxena, B. Sundman, J. Zhang, A thermodynamic assessment of silica phase diagram, Journal of Geophysical Research: Solid Earth 9)۹B6) (1994) 11787-11794.

[45] W.F. Hammetter, R.E. Loehman, Crystallization kinetics of a complex lithium silicate glass-ceramic, Journal of the American Ceramic Society 70(8) (1987) 577-582.

[46] F. Al-Saeedi, D.P. Danilovich, E.V. Kolobkova, The effect of nucleating temperature on the crystallization, phase formation and properties of lithium aluminum silicate (LAS) glass-ceramics, Ceramics International 50(7) (2024) 12434-12442.

[47] S. Huang, Z. Zujovic, Z. Huang, W. Gao, P. Cao, Crystallization of a high-strength lithium disilicate glass-ceramic: An XRD and solid-state NMR investigation, Journal of Non-Crystalline Solids 457 (2017) 65-72.

[48] B.d.F. Vallerini, L.D. Silva, M. de OC Villas-Bôas, O. Peitl, E.D. Zanotto, L.A. Pinelli, Microstructure and mechanical properties of an experimental lithium disilicate dental glass-ceramic, Ceramics International 50(1) (2024) 188-196.





[ DOI: 10.22068/ijmse.4363 ]

[49] F. Lodesani, M.C. Menziani, K. Maeda, Y. Takato, S. Urata, A. Pedone, Disclosing crystal nucleation mechanism in lithium disilicate glass through molecular dynamics simulations and free-energy calculations, Scientific reports 10(1) (2020) 17867.

[50] W. Holand, G.H. Beall, Glass-Ceramic Technology, John Wiley & Sons2019.





[ DOI: 10.22068/ijmse.4363 ]